


## Research article

# Solidified Tailings-Contaminated Sludge as an Anti-Seepage Material for Solid Waste Landfills: Mechanical Characteristics and Microscopic Mechanisms

Lianjie Mao<sup>1</sup>, Wanyuan Cui<sup>1</sup>, Ming Chen<sup>2</sup>, Haijun Lu<sup>1</sup>

<sup>1</sup> School of Civil Engineering and Architecture, Wuhan Polytechnic University, Wuhan 430023, China

<sup>2</sup> Hubei Institute of Urban Geological Engineering, Wuhan 430050, China

### Keywords:

Solid waste landfill  
impermeable materials  
curing agents  
mechanical properties  
C-S-H gel

### Cited as:

Mao LJ, Cui WY, Chen M, et al. 2025. Solidified Tailings-Contaminated Sludge as an Anti-Seepage Material for Solid Waste Landfills: Mechanical Characteristics and Microscopic Mechanisms. *GeoStorage*, 1(2), 171-179. <https://doi.org/10.46690/gs.2025.02.06>

### Abstract:

This study utilizes an industrial solid-waste composite consolidant (CSGA) to stabilize mine tailings sludge for the development of impermeable materials in solid waste landfills. The evolution of mechanical properties and micro-reaction mechanisms during sludge consolidation was systematically investigated. Unconfined compressive strength and permeability coefficients under varying consolidant dosages and curing periods were determined through unconfined compressive strength tests and flexible-wall permeability tests. FTIR, BET, and TG-DTG characterization techniques were employed to analyze the chemical functional groups, pore structure, and surface micromorphology of the consolidated sludge. The unconfined compressive strength increased markedly with higher consolidant dosages and longer curing periods, reaching 4.61 MPa at 7 days, while the 14-day strength was 73.43% higher than that at 7 days. After 28 days of curing, the permeability coefficient ranged between  $5.01 \times 10^{-8}$  and  $6.74 \times 10^{-8}$  cm/s. Substantial amounts of C-S-H or C-A-S-H gels, calcium hydroxide, and ettringite (Aft) formed in the consolidated sludge, and some  $\text{Ca}(\text{OH})_2$  underwent carbonation during the later curing stages to produce  $\text{CaCO}_3$  that filled internal pores. The synergistic action of NaOH, calcium lignosulfonate, and urea enhanced the reactivity of active components in the industrial solid waste and sludge, promoting gel formation and microstructural densification. This study provides a scientific basis for the design and construction of impermeable materials for mine-tailings-sludge-based landfills.

## 1 Introduction

Silt, a common solid waste characterized by high water content and rich organic matter, primarily originates from processes such as river and lake dredging, reservoir sediment removal, and municipal sewage treatment. Its production has been increasing annually with the acceleration of urbanization and the expansion of water conservancy projects (Chen et al., 2024; Dong et al., 2022). Statistics indicate that the global stock of reservoir silt exceeds 100 billion tons, with my country producing hundreds of millions of tons annually due to water system management and municipal engineering projects. However, disposal methods primarily involve simple landfilling and stockpiling (Wang et al., 2019; Liu et al., 2025),

resulting in a resource utilization rate of less than 30%. This not only occupies substantial land resources but also leads to secondary pollution, significantly hindering water environment management and sustainable urban development (Chetri and Reddy, 2021). Therefore, the efficient treatment and utilization of silt are directly linked to environmental protection and the sustainable development of the construction and water conservancy industries (Han et al., 2020).

Current sludge treatment technologies primarily include solidification and stabilization, heat treatment, modified sintering, and biological disposal (Huang et al., 2023). Among these, solidification is widely employed due to its straightforward pro-

cess, moderate cost, and broad applicability, showing promising potential, particularly in engineering fills, road base courses, and building material preparation (Hou et al., 2025). International research on sludge solidification agents has focused on mineral admixtures such as cement, lime, and fly ash for solidification (Chen et al., 2021). Concurrently, the synergistic use of industrial byproducts, such as phosphogypsum, slag, and silica fume, is being explored (Corrêa-Silva et al., 2020) to enhance mechanical properties and reduce costs. This approach is gradually shifting towards ecological security and carbon emission reduction, with a focus on the long-term stability of the solidified matrix and the retention mechanisms of heavy metals (Dong et al., 2025).

A survey by the Ministry of Housing and Urban-Rural Development of China on the operation of solid waste landfills revealed that traditional compacted clay closure systems often suffer from defects such as cracking and difficulty in soil extraction (Guo et al., 2020; Liu et al., 2022), while HDPE geomembranes are prone to tearing and bulging (Duan et al., 2021; Feng et al., 2023). Based on this, the study employs an industrial solid-waste composite solidifier (CSGA), synergistically prepared using an alkali activator and mineral admixtures, to solidify tailings sludge and produce impermeable materials for solid waste landfills. Unconfined compressive strength and flexible-wall permeability tests, along with multi-scale characterization methods such as FT-IR, BET, and TG-DTG, were used to systematically elucidate the macroscopic mechanical characteristics and reaction mechanisms of the CSGA-solidified sludge system, providing a scientific basis and technical support for sludge resource utilization and the development of sludge-based impermeable materials for landfills.

## 2 Experimental materials and methods

### 2.1 Experimental materials

Tailings sludge was sourced from an iron tailings accumulation area in Qichun County, Huanggang City, Hubei Province. It was primarily dark gray, with some lumps, a moisture content of 32.62%, and a specific surface area of 3150 cm<sup>2</sup>/g. Its primary components are presented in Tab.1.

Gypsum powder was sourced from a chemical plant in Wuhan, Hubei Province. It was a grayish-black powder with some lumps and an initial moisture content of 10.50%. Its primary component was calcium sulfate dihydrate. Prior to the experiment, the undisturbed gypsum powder was dried to a constant weight in a 105°C forced-air drying oven (DHG-9145A, Shanghai Heheng Instrument Equipment Co., Ltd., China), ground, and passed through a 60-mesh sieve for subsequent use. Slag, cement, and steel slag powders were purchased from a building materials company in Anhui Province. The slag was of grade S95, a white powder with a particle size range of 1-60 μm; the cement was of grade C42.5, a grayish-brown powder with a particle size of 80 μm. Caustic soda was purchased from a chemical company in Tianjin, China, in the form of a white, flaky solid. Calcium lignosulfonate and urea were produced by Guangdong Guanghua Science & Technology Co., Ltd., China, using analytical-grade reagents.

### 2.2 CSGA preparation and experimental methods

A composite alkali activator containing calcium lignosulfonate, urea, and caustic soda was blended with dried gypsum powder, slag, steel slag powder, and cement. The resulting mixture was subsequently milled for 20 min at 300 r/min in a vertical planetary ball mill (XQM-4, Jiangxi Victor International Mining Equipment Co., Ltd., China) to obtain the industrial solid-waste composite curing agent (CSGA) powder.

Three groups of solidified sludge specimens were prepared using CSGA dosages of 12%, 16%, and 20%, and designated as groups A, B, and C. The sludge and corresponding CSGA dosages were placed in a cement paste mixer (JJ-5, Shandong Yisheng Heavy Industry Technology Co., Ltd., China), mixed at low speed for 45 s and then at high speed for an additional 45 s until homogeneous. Deionized water was gradually added during mixing to maintain the optimal moisture content, followed by mechanical stirring for 2 min until a uniform mixture was obtained. The mixture was poured into cylindrical molds (50 mm × 50 mm) and compacted at a loading rate of 40 kN/min. After maintaining the load for 40 s, the specimens were demolded, labeled, and placed in a standard curing chamber at 20 ± 2°C and a relative humidity above 95%. The curing periods were 7, 14, and 28 days, during which the specimens were periodically rotated to minimize moisture gradients caused by gravity and evaporation. After curing, the specimens were dried in a 60°C forced-air oven (DHG-9145A, Shanghai Heheng Instrument Equipment Co., Ltd., China) until a constant weight was reached. A flowchart of the specimen preparation process is shown in Fig. 1.

Compressive strength tests were conducted on specimens cured for 7, 14 and 28 days. In accordance with Chinese standard GB/T 17671-2021, compressive strength was measured using a fully automatic microcomputer-controlled electro-hydraulic servo testing machine (DYE-300S, Yice Instrument Equipment (Hebei) Co., Ltd., China). The peak failure load was recorded, and compressive strength was calculated based on the loaded area.

Taking the 28-day cured specimens as the research objects, flexible-wall permeability tests were conducted on the solidified sludge. In accordance with the Geotechnical Test Code (GB/T 50123-1999), all specimens were vacuum-saturated prior to testing. Cylindrical samples with a diameter of 5 cm and a height of 10 cm were placed in a BHG vacuum saturation chamber (Nanjing Jingke Yusheng Instrument Co., China), evacuated for 24 h, and then immersed in water within the chamber for 48 h to achieve full saturation. Following ASTM D5084-03, permeability tests were performed using an environmental geotechnical flexible-wall permeameter (PN3230M, GEOEQUIP, USA). The confining pressure was set to 300 kPa, and the back pressure during permeation was maintained at 30 kPa.

Fourier transform infrared (FTIR) spectroscopy was performed using a Thermo Scientific Nicolet 10 spectrometer (Thermo Fisher Scientific, USA) to characterize the samples. During the measurement, the spectral scanning range was set to 4000–400 cm<sup>-1</sup>, with 32 scans conducted at a resolution of 2

**Tab. 1** Major chemical composition of tailings sludge (wt%)

Chemical composition	CaO	SO <sub>3</sub>	SiO <sub>2</sub>	Fe <sub>2</sub> O <sub>3</sub>	Al <sub>2</sub> O <sub>3</sub>	MgO	Others
Tailings sludge	5.29	0.46	59.68	7.90	18.48	1.77	6.42

**Fig. 1** Flow chart of the solidified body preparation process

cm<sup>-1</sup>.

The BET specific surface area was measured using an AUTOSORB-1-C analyzer (Quantachrome, USA), with nitrogen employed as the adsorbate to characterize the specific surface area and pore structure of the samples. Prior to testing, the samples were degassed at 200 °C for 6 h.

Thermogravimetric–differential thermal analysis (TG–DTG) was performed on samples cured for 7 and 14 days, and the resulting curves (Fig. 6) were used to analyze the phase transition behavior of the specimens. A synchronous thermal analyzer (STA449F5, Netzsch Scientific Instruments Trading (Shanghai) Co., Ltd., Germany) was used, with a heating range of 30–1300 °C and a heating rate of 10 °C/min.

### 3 Results and discussion

#### 3.1 Macroscopic mechanical properties

As illustrated in Fig. 2, the compressive strength of specimens with different curing-agent dosages and curing ages exhibits a pronounced increasing trend. For the 7-day specimens, compressive strength increased with higher curing-agent dosages: samples A, B, and C exhibited strengths of 2.579 MPa, 3.82 MPa, and 4.61 MPa, respectively (Fig. 2(a)). This suggests that higher dosages enhance the NaOH activation effect, promoting the dissolution of reactive Si and Al in the mineral powder and steel slag and generating larger quantities of C–S–H and

C–A–S–H gels. These gels provide early-stage filling and cementation, gradually densifying the solidified matrix. By 14 days, mechanical strength further increased, with samples A, B, and C reaching 4.22 MPa, 5.16 MPa, and 7.995 MPa, respectively (Fig. 2(b)), representing increases of approximately 1.35–1.73 times—substantially higher than those observed at 7 days. This indicates that hydration and activation reactions continued between 7 and 14 days, accompanied by further accumulation of C–S–H gels and calcium hydroxide, ongoing pore filling, and a structural transformation from a loose to a dense matrix. These processes contributed to the formation of a stable, continuous cemented skeleton, providing a robust microscopic basis for the observed improvement in macroscopic mechanical strength (Shu et al., 2022). After 28 days of curing, the compressive strengths of specimens A, B, and C were 3.973 MPa, 4.767 MPa, and 6.845 MPa, respectively (Fig. 2(c)), which were slightly lower than those measured at 14 days. This reduction may be attributed to intense early hydration reactions driven by strong alkaline activation, which produced substantial quantities of metastable hydration products. During later curing stages, these products underwent structural reorganization and transformation, thereby reducing the resulting mechanical strength.

The hydraulic conductivity of the solidified tailings sludge are presented in Fig. 3. As shown in Fig. 3, after 28 days of

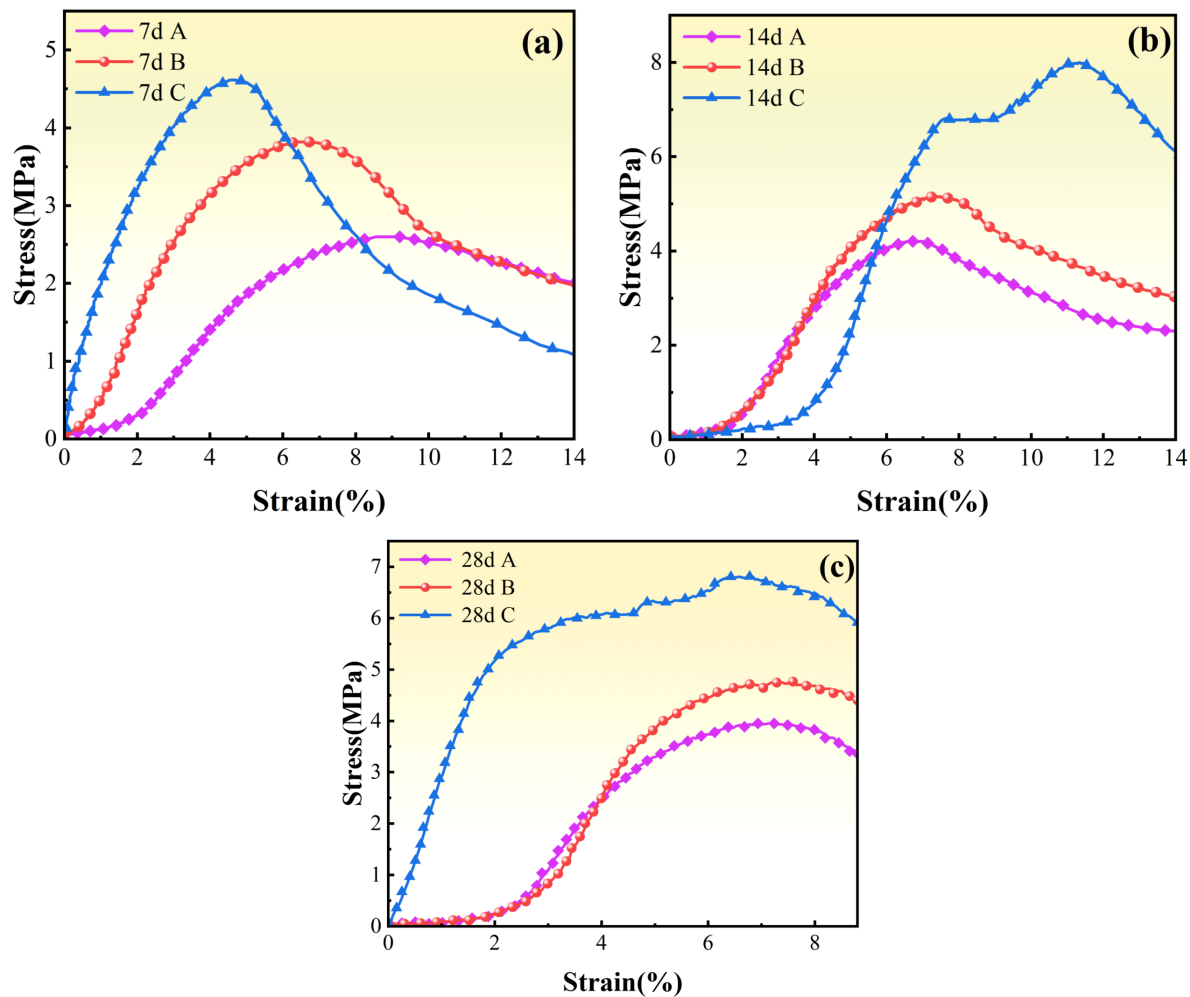


**Fig. 2** Unconfined compressive strength of solidified sludge cured for 7, 14 and 28 days

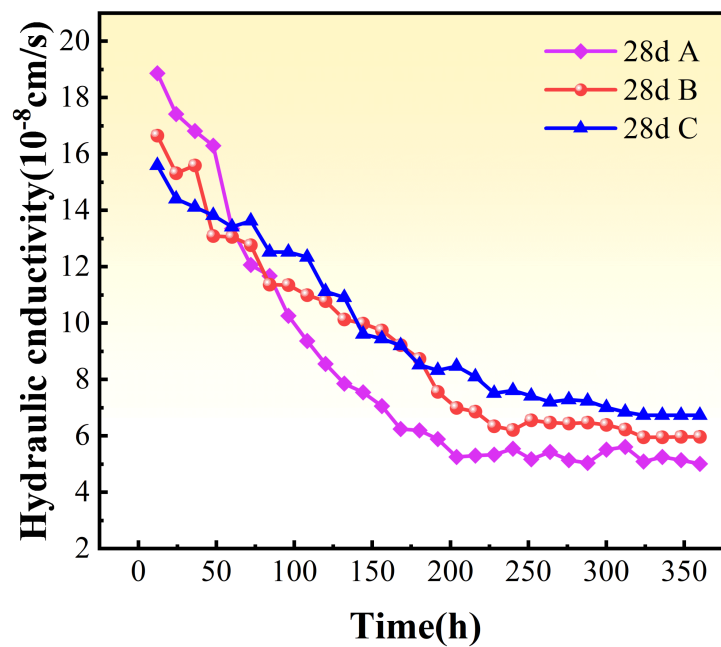


**Fig. 3** Hydraulic conductivity of the solidified sludge



curing, samples A, B, and C exhibited hydraulic conductivity of  $5.01 \times 10^{-8}$  cm/s,  $5.97 \times 10^{-8}$  cm/s, and  $6.74 \times 10^{-8}$  cm/s, respectively. These values meet the engineering requirements for impermeable materials specified in the Standard for Pollution Control of General Industrial Solid Waste Storage and Landfill (GB 18599-2020).

## 3.2 Microscopic characterization

### 3.2.1 Functional group structure

The infrared spectra of the 7-day specimens are shown in Fig.4(a). The absorption peak at  $3615\text{--}3693\text{ cm}^{-1}$  corresponds to the O-H stretching vibration of calcium hydroxide, indicating substantial  $\text{Ca}(\text{OH})_2$  formation in the system. The broad peak at  $3430\text{--}3433\text{ cm}^{-1}$  and the bending peak at  $1635\text{--}1656\text{ cm}^{-1}$  correspond to the -OH stretching and H-O-H bending vibrations, respectively, reflecting the presence of bound and adsorbed water in the hydration products (Wu et al., 2023). The main peak at  $1010\text{--}1040\text{ cm}^{-1}$  represents the asymmetric Si-O-Si/Al stretching vibration associated with the C-S-H/C-A-S-H gel skeleton formed from mineral powder and steel-slag powder under NaOH activation. Its intensity increases with higher curing-agent dosages and longer curing periods, indicating continuous advancement of hydration and gel-polymerization processes.

The shoulder peak near  $1105\text{ cm}^{-1}$  corresponds to the  $\text{SO}_4^{2-}$  vibration, indicating gypsum participation in Aft/AFm formation, whereas the band at  $1427\text{--}1463\text{ cm}^{-1}$  corresponds to the antisymmetric  $\text{CO}_3^{2-}$  (C-O) stretching vibration, suggesting carbonation of part of the  $\text{Ca}(\text{OH})_2$  to form  $\text{CaCO}_3$  (Wu et al., 2020). When the curing period was extended from 7 to 14 days (Fig.4(b)), the Si-O-Si/Al, OH, and  $\text{SO}_4^{2-}$  peaks increased in intensity and became sharper (Xiao et al., 2024). This indicates continued hydration, further accumulation of C-S-H gels and  $\text{Ca}(\text{OH})_2$ , progressive microstructural densification, and pore filling by  $\text{CaCO}_3$ . These results further demonstrate that higher curing-agent dosages effectively activate the potential reactive components through the synergistic NaOH-gypsum activation mechanism, thereby promoting the accumulation of cementitious products and enhancing the macroscopic strength of the system.

### 3.2.2 Specific surface area and pore size distribution

Fig.5 presents the adsorption-desorption curves for two groups of specimens at different curing ages, and Tab.3 lists the corresponding BET specific surface area and pore size distribution results.

Fig.5(a) shows that the isothermal adsorption-desorption curves of all 7-day specimens exhibit typical Type IV characteristics, indicating the formation of a hierarchical pore structure dominated by capillaries and mesopores in the cured product. As the dosage of the curing agent increased from 12% to 20%, the specific surface area and total pore volume of the samples increased significantly. Meanwhile, as shown in Fig.5(b), the pore size distribution curves shifted overall within the 10–100 nm range, with the 7-day C sample exhibiting a pronounced peak in the 20–40 nm range. This indicates that under high-dosage conditions, the synergistic activation of NaOH and  $\text{Ca}^{2+}$  significantly enhances the potential reactivity of the mineral

powder and steel slag, leading to the formation of a large amount of gel products such as C-S-H and Aft. These products are not fully cross-linked in the early stages, creating more open mesopores and gel pores, thereby increasing the specific surface area and pore volume (Dong et al., 2025). Although the pore structure is relatively developed at this stage, the gel phase has not fully filled the pores, and the microstructure remains relatively loose, leading to an increase in macroscopic compressive strength without reaching its peak (Liu et al., 2023).

Fig.5(c) shows a decrease in hysteresis loop area and a slowing of the overall increase in the adsorption-desorption curves at 14 days, indicating that pores in the system are gradually filled by later hydration products and become denser. The specific surface area and pore volume of all three samples slightly decreased compared with the 7-day samples, while the pore size distribution peaks, as shown in Fig.5(d), shifted overall toward the larger pore size range of 20–40 nm. The 14-day C sample still maintained the highest pore volume and specific surface area. This suggests that in the high-doping system, although gel continues to form and fill some pores, some large or interconnected pores are reshaped due to intense hydration reactions, resulting in a typical multi-scale pore structure (Liu et al., 2022). This structure not only facilitates the diffusion and continued growth of hydration products but also maintains a high specific surface area, enhancing interfacial adhesion and strength development (Metwally et al., 2025). As the curing period progresses, the pores in the system gradually transform from open and porous to dense and continuous. The high curing-agent dosage promotes more complete activation and gel filling, forming a denser micro-skeleton and enabling the macroscopic compressive strength to reach its peak.

### 3.2.3 Thermal effect test analysis

For the 7-day solidified sludge samples (Fig. 6(a)), the TG curves exhibited a continuous mass-loss trend with increasing temperature, primarily attributable to free-water evaporation, bound-water removal, and decomposition of hydration products and solidified phases. Among these samples, 7d-C displayed the highest mass-loss rate (11.87%), indicating greater quantities of thermally decomposable hydration phases and gel products (Miraki et al. 2022), whereas 7d-A showed the highest mass retention (91.65%), suggesting incomplete hydration and the presence of unreacted components or physically adsorbed water. The DTG curves show that the weight-loss peak at  $100\text{--}200^\circ\text{C}$  corresponds to dehydration of chemically bound water and C-S-H gel; with increasing curing-agent dosage, the peak intensity increases slightly, indicating enhanced C-S-H formation (Ramadan et al., 2023). The pronounced peak in the  $400\text{--}600^\circ\text{C}$  range corresponds to  $\text{Ca}(\text{OH})_2$  decomposition, with the sharper peak of sample 7d-C indicating higher  $\text{Ca}(\text{OH})_2$  content and increased system alkalinity, promoting activation of potentially reactive minerals. The weak peak at  $600\text{--}800^\circ\text{C}$  corresponds to  $\text{CaCO}_3$  decomposition, with low intensity for all samples, indicating limited carbonation within 7 days.

For the 14-day samples (Fig. 6(b)), the TG curves likewise exhibited a continuous mass-loss trend. Sample 14d-C showed the highest mass-loss rate across the temperature range, indicating greater amounts of thermally unstable hydration prod-

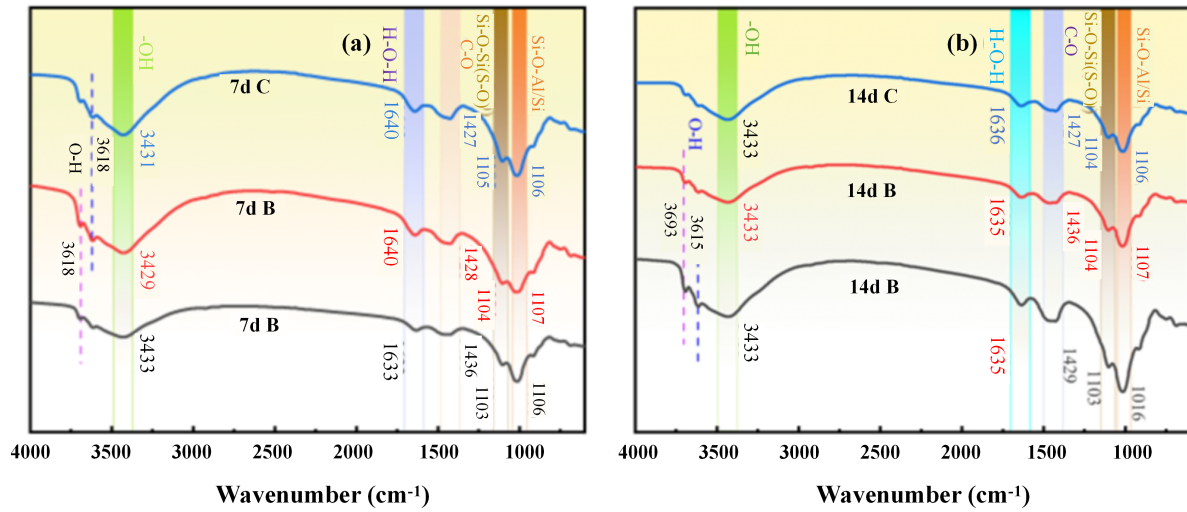


Fig. 4 FTIR spectra of the samples cured for 7 days (a) and 14 days (b)

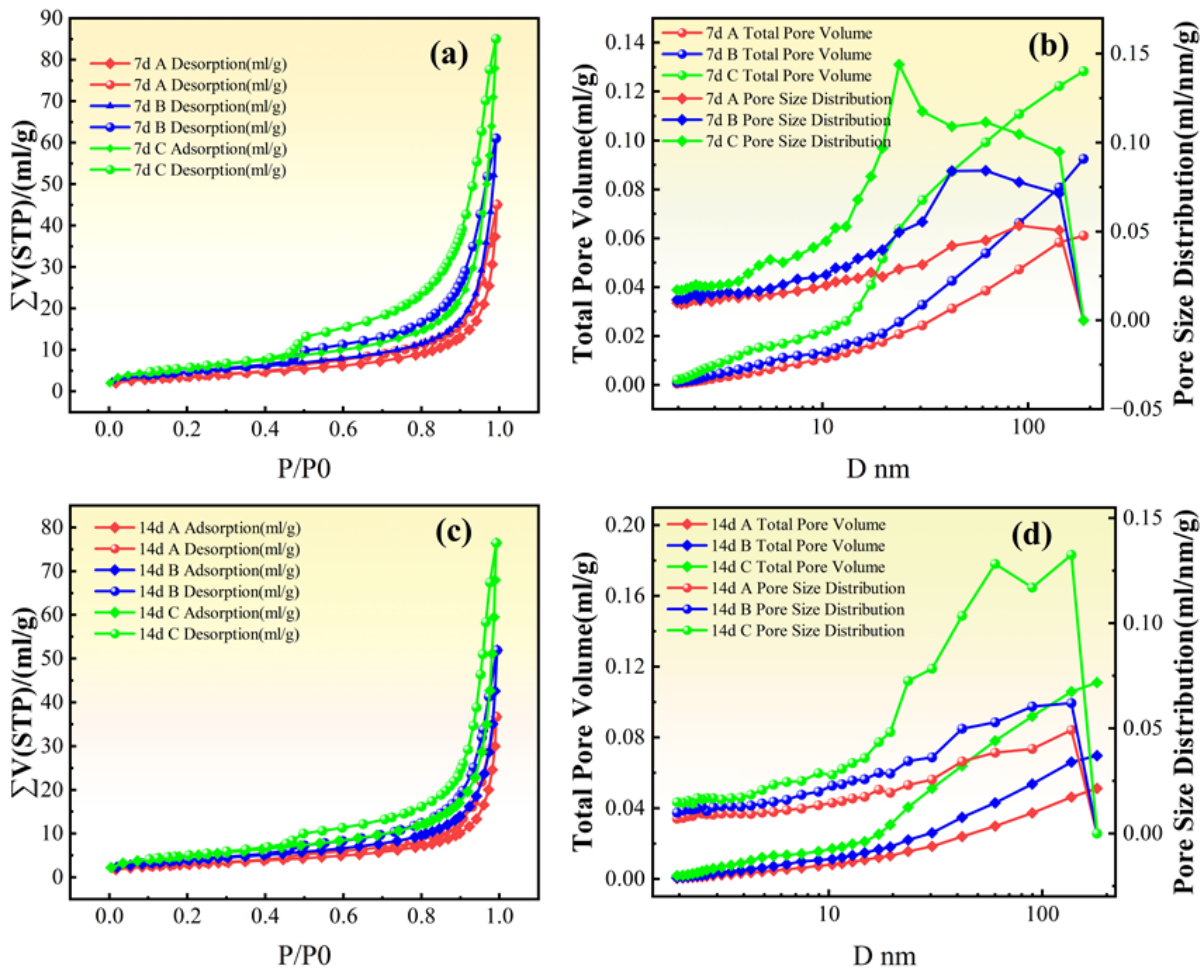


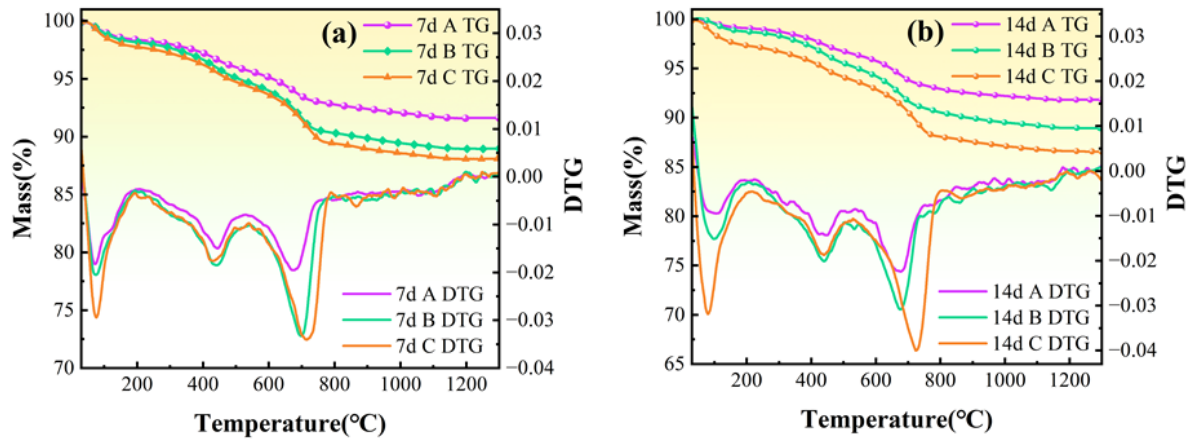
Fig. 5 BET adsorption-desorption isotherms of the samples cured for 7 days (a) and 14 days (b)

ucts and gel phases. The DTG curves reveal that the peak for sample 14d-C was sharper, with a larger area and a shift toward higher temperatures, signifying continued hydration and alkali-activation reactions and progressive structural densification. The intensified low-temperature dehydration peak

reflects increased C-S-H and AFt content, the strengthened mid-temperature  $\text{Ca}(\text{OH})_2$  decomposition peak indicates higher  $\text{Ca}(\text{OH})_2$  formation, and the more prominent high-temperature  $\text{CaCO}_3$  decomposition peak indicates increased carbonation (Shi et al., 2023). Overall, increasing curing-agent dosage

**Tab. 2** Summary of the specific surface area of the samples cured for 7 and 14 days

Sample	Specific surface area (m <sup>2</sup> /g)	Total pore volume (cm <sup>3</sup> /g)	Average pore diameter (nm)
7d A	13.1512	0.0605	18.4014
7d B	16.9036	0.0918	21.7232
7d C	20.9068	0.1263	24.1644
14d A	10.7234	0.0510	19.0238
14d B	14.2073	0.0694	19.5393
14d C	17.9542	0.1101	24.5291

**Fig. 6** TG-DTG curves of the samples cured for 7 days (a) and 14 days (b)

and curing age intensified hydration and activation reactions, increased cementitious product formation, densified the microstructure, and consequently enhanced macroscopic strength.

### 3.3 Hydration mechanism

Under the strongly alkaline environment provided by NaOH in the masterbatch, the disordered glassy structure in the mineral and steel slag powders is eroded by OH<sup>-</sup>, dissolving a large number of active silicate and aluminate ions, which serve as precursors for the subsequent gelation reaction. Simultaneously, cement hydration rapidly generates C-S-H gel and Ca(OH)<sub>2</sub>, which, on one hand, builds early strength, while on the other hand, maintains the high pH of the system, facilitating the continuous dissolution of additional Si/Al active components (Song et al., 2025). The dissolved SiO<sub>4</sub><sup>4-</sup>/Al(OH)<sub>4</sub> further polymerize with Ca<sup>2+</sup> in the system to form C-S-H and C-A-S-H gels. These amorphous gels intertwine and fill the pores, providing the primary source of final strength (Sun et al., 2020).

Gypsum reacts with aluminate and Ca<sup>2+</sup> in solution, releasing SO<sub>4</sub><sup>2-</sup> to form needle-like ettringite. The micro-expansion of ettringite fills pores, enhancing structural density. Simultaneously, AFt formation continuously consumes the aluminum phase, disrupting ionic equilibrium and promoting the dissolution of additional active phases from the mineral powder/steel slag, thereby achieving a “synergistic activation” effect. As aging time increases, hydration products continually fill and reconstruct the pore structure, gradually transforming the early-stage loose porous framework into a dense, continuous network. Subsequent carbonation further transforms Ca(OH)<sub>2</sub> into fine CaCO<sub>3</sub> crystals, providing secondary filling and shifting the pore size distribution from interconnected macropores to fine gel pores (Wang et al., 2021). Ultimately, the gel phase, AFt

crystals, and calcium carbonate collectively form a highly dense microstructure, significantly enhancing the strength and long-term stability of the solidified sludge. The microscopic mechanism is illustrated in Fig. 7.

### 4 Conclusions

This study employed an industrial solid waste composite solidifier (CSGA) to solidify tailings sludge and combined it with unconfined compressive strength and permeability tests, as well as microscopic characterization methods such as FTIR, BET, and TG-DTG, to draw the following conclusions:

- The industrial solid waste composite solidifier (CSGA) significantly improves the unconfined compressive strength of solidified sludge, with strength continuing to increase with higher dosages and extended curing times. After 14 days of curing, the strength of the solidified body with a 20% dosage reaches 7.995 MPa, indicating that the solidifier can efficiently form high-load-bearing structural materials.
- A significant synergistic activation effect exists between NaOH and gypsum. NaOH strongly activates the potential reactivity of mineral powder and steel slag, dissolving silicon and aluminum components, while gypsum promotes AFt crystal formation to fill pores and accelerates the dissolution and reaction of active components by consuming the aluminum phase, jointly promoting large-scale generation of C-S-H and C-A-S-H gels.
- The multi-scale porous structure formed early in the solidified body is effectively filled by the continuously generated gel products and crystals (e.g., AFt, CaCO<sub>3</sub>) in the later stages, resulting in a decrease in specific surface area and total pore volume, refinement of pore size, and the



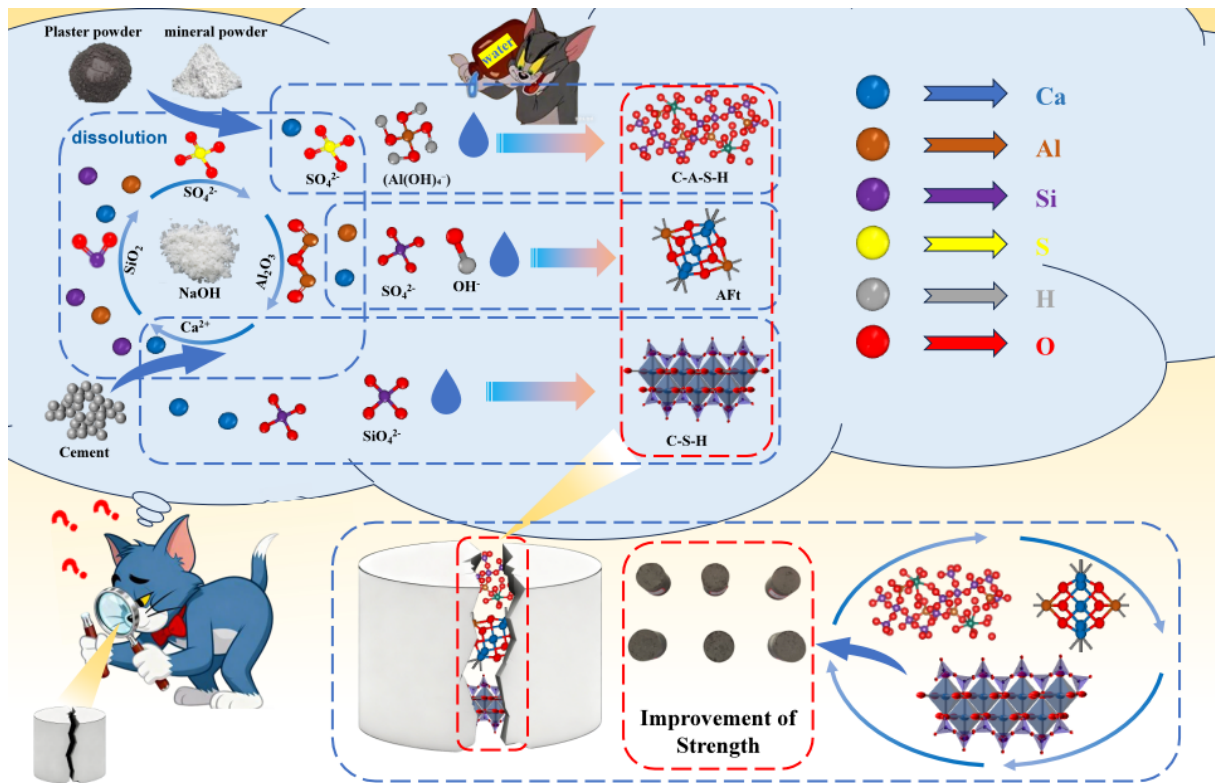


Fig. 7 Schematic illustration of the microscopic mechanism

formation of a dense, continuous solid skeleton, which is the primary reason for the increase in macroscopic strength.

- The hydration products in the curing system exhibit diverse and synergistic properties. C-S-H/C-A-S-H gels, as the primary cementing phase, form a three-dimensional network; AFt crystals are interspersed, filling and reinforcing the structure; and CaCO<sub>2</sub>, a carbonation product of Ca(OH)<sub>2</sub>, further refines micropore filling. Together, these products constitute the strength foundation and stability assurance of the cured body.

The CSGA used in this study incorporates industrial solid waste (mineral powder, steel slag, gypsum) as its primary raw materials, effectively reducing cement usage and carbon emissions. While achieving sludge harmlessness and solidification, it also offers excellent mechanical properties and environmental benefits, providing a practical and feasible solution for sludge-based seepage prevention materials and the resource utilization of various industrial solid wastes.

## Acknowledgements

This work was financially supported by Major Innovation Projects of Hubei Province, P. C. China (2024BCB081).

## Conflict of interest

The authors declare no competing interest.

**Open Access** This article is distributed under the terms and conditions of the Creative Commons Attribution (CC BY-NC-ND) license, which permits unrestricted use, distribution, and reproduction in any medium, provided the original work is properly cited.

## References

- Chen ZZ, You NQ, Chen C, et al. 2021. Properties of dredged sludge solidified with alkali-activated slag-based materials and blended with copper slag as fine aggregates of mortars. *Construction and Building Materials*, **312**: 125459. doi:10.1016/j.conbuildmat.2021.125459.
- Chen ML, Wu DZ, Chen KY, et al. 2024. The influence of fly ash-based geopolymers on the mechanical properties of OPC-solidified soil. *Construction and Building Materials*, **432**: 136591. doi:10.1016/j.conbuildmat.2024.136591.
- Chetri JK, Reddy KR. 2021. Advancements in Municipal Solid Waste Landfill Cover System: A Review. *Journal of the Indian Institute of Science*, **101**(4): 557–588. doi:10.1007/s41745-021-00229-1.
- Corrêa-Silva M, Miranda T, Rouainia M, et al. 2020. Geomechanical behaviour of a soft soil stabilised with alkali-activated blast-furnace slags. *Journal of Cleaner Production*, **267**: 122017. doi:10.1016/j.jclepro.2020.122017.
- Dong WY, Gu WY, Zhan QW, et al. 2022. Study on the Property and Mechanism of Low Content Cement-Industrial Waste Residue Silt Solidification. *Science of Advanced Materials*, **14**(12): 1881–1892. doi:10.1166/sam.2022.4388.
- Dong M, Wen XD, Lang L, et al. 2025. Enhanced early strength and microstructural stability of dredged sludge using CPC-S curing agent. *Construction and Building Materials*, **466**: 140219. doi:10.1016/j.conbuildmat.2025.140219.
- Duan WJ, Wang DG, Wang ZM, et al. 2021. A novel synergistic method on potential green and high value-added utilization of blast furnace slag. *Journal of Cleaner Production*, **329**: 129804. doi:10.1016/j.jclepro.2021.129804.
- Feng DL, Wang J, Wang YX, et al. 2023. Experimental study on solidification/stabilisation of high-salt sludge by alkali-activated GGBS and MSWI bottom ash cementitious mate-



- rials. *Case Studies in Construction Materials*, **19**: e02417. doi:10.1016/j.cscm.2023.e02417.
- Guo ZG, Jiang T, Zhang J, et al. 2020. Mechanical and durability properties of sustainable self-compacting concrete with recycled concrete aggregate and fly ash, slag and silica fume. *Construction and Building Materials*, **231**: 117115. doi:10.1016/j.conbuildmat.2019.117115.
- Han FH, Zhou Y, Zhang ZQ. 2020. Effect of gypsum on the properties of composite binder containing high-volume slag and iron tailing powder. *Construction and Building Materials*, **252**: 119023. doi:10.1016/j.conbuildmat.2020.119023.
- Hou WJ, Ye F, Yu Y, et al. 2025. Experimental study on the strength characteristics and seawater degradation resistance of sandy silt solidified with alkali-activated slag. *Construction and Building Materials*, **458**: 139610. doi:10.1016/j.conbuildmat.2024.139610.
- Huang L, Geng JG, Chen MY, et al. 2023. Investigation into the Rheological Properties and Microstructure of Silt/Crumb Rubber Compound-Modified Asphalt. *Polymers*, **15**(11): 2474. doi:10.3390/polym15112474.
- Liu JJ, Yang CH, Song R, et al. 2025. Advances of Geological Storage Engineering and Technology. *GeoStorage*, **1**(1): 1–26. doi:10.46690/gs.2025.01.01.
- Liu MY, Lu HJ, Deng QK, et al. 2022. Shear strength, water permeability and microstructure of modified municipal sludge based on industrial solid waste containing calcium used as landfill cover materials. *Waste Management*, **145**: 20–28. doi:10.1016/j.wasman.2022.04.031.
- Liu Y, Lu HJ, Liu MY, et al. 2022. Microanalytical characterizations, mechanical strength and water resistance performance of solidified dredged sludge with industrial solid waste and architecture residue soil. *Case Studies in Construction Materials*, **17**: e01492. doi:10.1016/j.cscm.2022.e01492.
- Liu P, Mo LW, Zhang Z. 2023. Effects of carbonation degree on the hydration reactivity of steel slag in cement-based materials. *Construction and Building Materials*, **370**: 130653. doi:10.1016/j.conbuildmat.2023.130653.
- Metwally GAM, Elemam WE, Mahdy M, et al. 2025. A comprehensive review of metakaolin-based ultra-high-performance geopolymer concrete enhanced with waste material additives. *Journal of Building Engineering*, **103**: 112019. doi:10.1016/j.jobe.2025.112019.
- Miraki H, Shariatmadari N, Ghadir P, et al. 2022. Clayey soil stabilization using alkali-activated volcanic ash and slag. *Journal of Rock Mechanics and Geotechnical Engineering*, **14**(2): 576–591. doi:10.1016/j.jrmge.2021.08.012.
- Ramadan M, Habib AO, Hazem MM, et al. 2023. Synergetic effects of hydrothermal treatment on the behavior of toxic sludge-modified geopolymer: Immobilization of cerium and lead, textural characteristics, and mechanical efficiency. *Construction and Building Materials*, **367**: 130249. doi:10.1016/j.conbuildmat.2022.130249.
- Shi XM, Xu HQ, Zhang N, et al. 2023. Study on semi-dynamic leaching and microstructure characteristics of MSWI fly ash solidified sediment. *Journal of Environmental Management*, **348**: 119405. doi:10.1016/j.jenvman.2023.119405.
- Shu BN, Chen WZ, Yang TY, et al. 2022. Study on laboratory and engineering application of multi source solid waste based soft soil solidification materials. *Case Studies in Construction Materials*, **17**: e01465. doi:10.1016/j.cscm.2022.e01465.
- Song YB, Zhang XP, Xu JX, et al. 2025. Mechanical properties and water resistance of alkali-activated flood-control stone incorporating ball-milling treated Yellow River silt. *Case Studies in Construction Materials*, **22**: e04640. doi:10.1016/j.cscm.2025.e04640.
- Sun HQ, Qian JS, Yang YL, et al. 2020. Optimization of gypsum and slag contents in blended cement containing slag. *Cement & Concrete Composites*, **112**: 103674. doi:10.1016/j.cemconcomp.2020.103674.
- Wang L, Yan DY, Xiong Y, et al. 2019. A review of the challenges and application of public-private partnership model in Chinese garbage disposal industry. *Journal of Cleaner Production*, **230**: 219–229. doi:10.1016/j.jclepro.2019.05.028.
- Wang DX, Zhu JY, Wang RH. 2021. Assessment of magnesium potassium phosphate cement for waste sludge solidification: Macro- and micro-analysis. *Journal of Cleaner Production*, **294**: 126365. doi:10.1016/j.jclepro.2021.126365.
- Wu S, Yao XL, Ren CZ, et al. 2020. Recycling phosphogypsum as a sole calcium oxide source in calcium sulfoaluminate cement and its environmental effects. *Journal of Environmental Management*, **271**: 110986. doi:10.1016/j.jenvman.2020.110986.
- Wu MM, Shen WG, Xiong X, et al. 2023. Effects of the phosphogypsum on the hydration and microstructure of alkali activated slag pastes. *Construction and Building Materials*, **368**: 130391. doi:10.1016/j.conbuildmat.2023.130391.
- Xiao Y, Tan YZ, Zhou CL, et al. 2024. Utilisation of silica-rich waste in eco phosphogypsum-based cementitious materials: Strength, microstructure, thermodynamics and CO<sub>2</sub> sequestration. *Construction and Building Materials*, **411**: 134469. doi:10.1016/j.conbuildmat.2023.134469.